Title

WNT1-induced Secreted Protein-1 (WISP1), a Novel Regulator of Bone Turnover and Wnt Signaling*

Journal

Journal of Biological Chemistry, 290(22)

ISSN

0021-9258

Authors

Maeda, Azusa
Ono, Mitsuaki
Holmbeck, Kenn
et al.

Publication Date

2015-05-01

DOI

10.1074/jbc.m114.628818

Peer reviewed

- Journal List
- J Biol Chem
- v.290(22); 2015 May 29
- PMC4447973

JBC JOURNAL OF BIOLOGICAL CHEMISTRY

Published by the American Society for Biochemistry and Molecular Biology

J Biol Chem. 2015 May 29; 290(22): 14004–14018.

Published online 2015 Apr 11. doi: 10.1074/jbc.M114.628818

PMCID: PMC4447973

PMID: 25864198

WNT1-induced Secreted Protein-1 (WISP1), a Novel Regulator of Bone Turnover and Wnt Signaling*

Azusa Maeda,[‡§] Mitsuaki Ono,[‡§] Kenn Holmbeck,[‡] Li Li,[‡] Tina M. Kilts,[‡] Vardit Kram,[‡] Megan L. Noonan,[‡] Yuya Yoshioka,[‡§] Erin M. B. McNerny,[¶] Margaret A. Tantillo,[¶] David H. Kohn,[¶] Karen M. Lyons,[‖] Pamela G. Robey,[‡] and Marian F. Young[‡,1]

Introduction

The extracellular matrix of bone is composed of multiple families of proteins, yet their precise functions in regulating bone formation and function have yet to be identified. The CCN family is named from its founding members (Cyr61, CTGF, Nov) and consists of six members now known as Cyr61/CCN1, CTGF/CCN2, Nov/CCN3, WISP1/CCN4, WISP2/CCN5, and WISP3/CCN6, which have diverse functions, including regulation of cell differentiation, proliferation, and migration (1). All six CCN members are found in the skeleton but with unique locations. For example, during normal skeletal development, CCN2 and CCN3 are highly expressed in cartilage (2), whereas CCN4 is largely confined to newly forming bone (3, 4). Considering that many of the CCN family members bind and regulate TGF-β, it is not surprising that they are being considered as potential therapeutic targets for diseases such as fibrosis, cancer, and osteoarthritis, in which TGF-β plays a crucial role in tissue pathology (1).

WISP1/CCN4 (hereafter referred to as WISP1) was first discovered as a target gene of the Wnt pathway, where it is aberrantly expressed in human colon cancer (5). Using a combination of *in situ* hybridization and immunohistochemistry, WISP1 was subsequently found highly expressed in osteoblasts and in perichondral mesenchyme (4). Further analysis showed that *Wisp1* is up-regulated in healing bone after induced fracture, indicating its important role in skeletal homeostasis (4). On the basis of these reports, we (6, 7) and others (8) began to examine the effect of WISP1 on osteoprogenitors and found that it can promote osteogenic differentiation when added exogenously to osteoprogenitor cells cultured *in vitro*. Despite this intriguing foundation, the exact roles of WISP1 in skeletal tissue *in vivo* have not been clearly elucidated.

To deepen our understanding of how WISP1 functions *in vivo*, we generated mice globally deficient in *Wisp1* and analyzed the structure and strength of their bones with aging. Our study points to a role for WISP1 in regulating many aspects of bone integrity, including the magnitude of peak bone mass, cortical thickness, and biomechanical strength, with an additional gender bias in bones from male and female mice. As we predicted, *Wisp1*-deficient osteoprogenitors differentiated poorly compared with WT counterparts both when induced *in vitro* and when implanted *in vivo* into immunocompromised mice. Further analysis showed that *Wisp1*$^{-/-}$ mice had increased osteoclastogenesis and that they were more sensitive to ovariectomy-induced bone loss compared with WT mice. The mechanistic foundation for these bone defects may arise in part from reduced levels of Wnt signaling, suggesting that WISP1, a target of Wnt, could engage in a feed-forward loop that simultaneously responds to and stimulates Wnt signaling during osteogenesis.

Experimental Procedures

Generation of Wisp1$^{-/-}$ *Mice*

Mice deficient in *Wisp1*$^{-/-}$ were generated using standard homologous recombination and gene targeting. Briefly, a 1.7-kb PGK-neo cassette, previously digested with XhoI and EcoRI, was inserted into an EcoRI site in exon 2 (see Fig. 1*A*). This insertion was predicted to cause a frameshift in the coding sequence of the WISP1 protein. The construct was transfected into murine embryonic stem (ES)[2] cells, and 400 G418-resistant clones were expanded and analyzed. Two ES clones, 3H4 and 4C5, were specifically targeted by the construct, determined by digestion of their DNA with ApaI, followed by Southern analysis using a 5′-external probe. Both ES clones were used for blastocyst injections. A PCR method for genotyping was designed using the following primers: *Wisp1* Exon2 R, 5′-AGCTGCTGGGCACATATCTT-3′; *Wisp1* Exon2 L, 5′-ACCCCCACAACAATGACCT-3′; and Neo, 5′-GTGCTTTACGGTATCGCCGCT-3′. For PCR, DNA extracted from tail biopsies was analyzed by gel electrophoresis. Two separate mouse lines were generated that retained germ line transmission of the targeted *Wisp1* allele. The creation and expansion of the *Wisp1*-deficient mice were carried out in the Gene Targeting Facility of the National Institutes of Health NIDCR Intramural Research Program under an institutionally approved protocol (09-536 and 10-562). The loss of WISP1 expression in the targeted mice was confirmed by Northern blotting, quantitative real-time PCR, and Western blotting, which are described in further detail below.

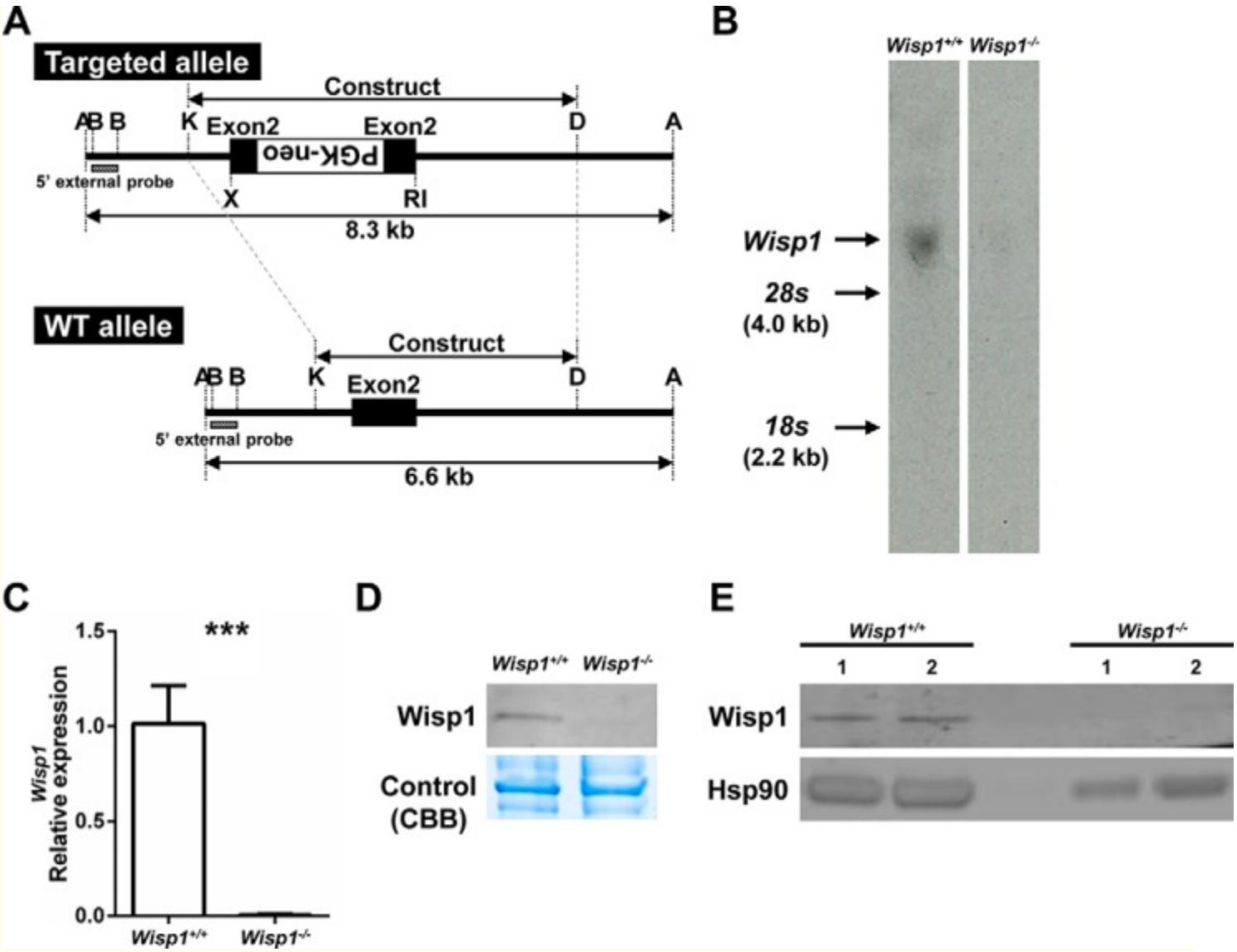

FIGURE 1.

Targeting strategy and confirmation of null allele. *A*, DNA construct used to target the mouse *Wisp1* gene and resulting targeted allele. *A*, ApaI; *B*, BglII; *RI*, EcoRI; *K*, KpnI; *D*, DpnI. *B*, Northern blotting of RNA derived from calvarial cells of 3-day-old mice. *C*, real-time PCR of mRNA extracted from osteogenic differentiated BMSCs. ***, $p < 0.001$ *versus* the wild-type (+/+) sample. *D*, Western blotting of protein extracted from hind limb bones for probing for *Wisp1* (*upper panel*) Coomassie Brilliant Blue (*CBB*) staining of the same gel was used to confirm equal loading (*lower panel*). *E*, Western blotting of two separate preparations of protein extracted from osteogenic differentiated WT or *Wisp1*$^{-/-}$ BMSCs while probing for *Wisp1*.

mRNA Analysis

RNA was extracted from calvarial osteoblasts of 3-day-old WT or *Wisp1*$^{-/-}$ mice and analyzed by Northern analysis using standard procedures. Briefly, 3 μg of mRNA was separated on a denaturing formaldehyde-agarose gel, transferred to nitrocellulose, and hybridized with a ^{32}P-labeled mouse *Wisp1* cDNA probe. Bands of the predicted size were identified after exposure to x-ray film.

Real-time RT-PCR

WT or *Wisp1*$^{-/-}$ bone marrow stromal cells (BMSCs) were cultured with osteogenic medium for 2 weeks, and mRNA was extracted using RNeasy (Qiagen). Next, cDNA was generated with an iScript cDNA

synthesis kit (170-8891, Bio-Rad). Real-time PCR was performed with the mouse-specific primers listed in Table 1 using iQ SYBR Green Supermix (170-8886, Bio-Rad) and a CFX96 real-time PCR detection system (Bio-Rad). Target gene expression was normalized using *S29*.

TABLE 1

Primer sequences used for real-time PCR

Gene	GenBank™ accession no.	Primer sequence	PCR product length (bp)
S29	NM_009093	5′-GGAGTCACCCACGGAAGTTCGG-3′ (sense)	108
		5′-GGAAGCACTGGCGGCACATG-3′ (antisense)	
Wisp1	NM_018865	5′-ATCGCCCGAGGTACGCAATAGG-3′ (sense)	142
		5′-CAGCCCACCGTGCCATCAATG-3′ (antisense)	
Col1a1	NM_007742	5′-CACCCTCAAGAGCCTGAGTC-3′ (sense)	269
		5′-GCTTCTTTTCCTTGGGGTTC-3′ (antisense)	
Alp	J02980	5′-GCTCTCCCTACCGACCCTGTTC-3′ (sense)	130
		5′-TGCTGGAAGTTGCCTGGACCTC-3′ (antisense)	
Bsp	NM_008318	5′-AAGTGAAGGAAAGCGACGAGGAAG-3′ (sense)	113

Gene	GenBank™ accession no.	Primer sequence	PCR product length (bp)
		5′-GTTGGTGCTGGTGCCGTTGAC-3′ (antisense)	
Ocn	NM_001032298	5′-CCAAGCAGGAGGGCAATAAGGTAG-3′ (sense)	122
		5′-CTCGTCACAAGCAGGGTCAAGC-3′ (antisense)	
Rankl	NM_011613	5′-TGAAGACACACTACCTGACTCCTG-3′ (sense)	198
		5′-CTGGCAGCATTGATGGTGAGG-3′ (antisense)	
Opg	NM_008764	5′-CCTTGCCCTGACCACTCTTATACG-3′ (sense)	140
		5′-CCTTCCTCACACTCACACACTCG-3′ (antisense)	
Axin2	NM_004655	5′-TGGAGAGTGAGCGGCAGAGC-3′ (sense)	89
		5′-TGGAGACGAGCGGGCAGAC-3′ (antisense)	
Ccnd1	NM_007631	5′-GCGTGGTGGCTGCGATGC-3′ (sense)	118
		5′-GAAAGAAAGTGCGTTGTGCGGTAG-3′ (antisense)	

Gene	GenBank™ accession no.	Primer sequence	PCR product length (bp)
Ctnnb1	NM_007614	5′-GCCGTTCGCCTTCATTATGGACTG-3′ (sense)	121
		5′-CTGGGCAAAGGGCAAGGTTTCG-3′ (antisense)	

Cell Culture

Mouse calvarial cells were isolated and cultured as described previously (9), and mouse BMSCs were harvested as reported previously (6). Briefly, cells were obtained from fresh bone marrow from femurs and tibias of 6–8-week-old female WT or *Wisp1*$^{-/-}$ mice and cultured with α-minimal essential medium (12571, Gibco) containing 20% lot-selected FBS (100-106, Gemini Bio Products, West Sacramento, CA), 2 mM glutamine (35050, Gibco), 100 units/ml penicillin, 100 μg/ml streptomycin (15140-122, Gibco), and 55 μM 2-mercaptoethanol (21985-023, Gibco). For osteoblastic differentiation, 10^{-8} M dexamethasone, 100 μM ascorbic acid 2-phosphate, and 2 mM β-glycerophosphate were added to normal medium. BMSCs plated in 6-well plates (5.0×10^5 cells/well) were cultured with the osteogenic differentiation medium for 1, 2, and 3 weeks, fixed, and stained with 2% Alizarin Red S (pH 4.2; Sigma) to detect Ca^{2+} accumulation. In some cultures, recombinant WISP1 (120-18, PeproTech, Rocky Hill, NJ) was added at a concentration of 100 ng/ml. The relative level of Ca^{2+} accumulation was quantified by elution of bound Alizarin Red with 0.5 ml of 5% SDS in 0.5 N HCl for 30 min at room temperature, and the absorbance was measured at 405 nm.

For the osteoclast cultures, cells were flushed from the bone marrow of tibias and femurs from 6–8-week-old female WT or *Wisp1*$^{-/-}$ mice, repeatedly pipetted to break up cell clusters, and placed into culture dishes with α-minimal essential medium containing 10% FBS, 100 units/ml penicillin, 100 μg/ml streptomycin (15070-063, Gibco), and 2.5 units/ml amphotericin (15290-026, Gibco). After 3 h, the non-adherent cells in the supernatant were transferred to a fresh culture plate. After overnight incubation, non-adherent cells containing osteoclast precursors were isolated, counted, and plated at a density of 1.65×10^5 cells/well in 96-well plate in medium supplemented with 30 ng/ml sRANKL (R&D Systems, Minneapolis, MN) and 20 ng/ml macrophage colony-stimulating factor (R&D Systems). The medium was replaced every 2 days and supplemented with fresh sRANKL and M-CSF. When giant osteoclasts appeared, cultures were fixed and stained with an acid phosphatase leukocyte (tartrate-resistant acid phosphatase (TRAP)) kit (387A-1KT, Sigma) and enumerated digitally using Image J.

Protein Extraction and Western Blotting

To examine the relative abundance of WISP1, tibias and femurs from 3-month-old WT and *Wisp1*$^{-/-}$ mice were dissected out and crushed to a fine powder with a FastPrep-24 instrument (20 s × 4 times at speed 6, 6004500, MP Biomedicals, Santa Ana, CA) using dry ice and a CoolPrep 24 × 2 ml adapter (116002-528, MP Biomedicals) with Lysing Matrix A (6910-050, MP Biomedicals). Guanidine (4 M) containing protease inhibitors was added to each sample and incubated for 20 min at room temperature to remove adherent soft tissue, after which the solution was changed to 0.5 M EDTA and incubated for 1 h. After sonication, gel loading buffer was added, the sample was boiled and centrifuged, and the supernatant was collected for gel analysis. In a second approach, protein was extracted from WT and *Wisp1*$^{-/-}$ BMSCs previously cultured with osteogenic medium for 2 weeks, and protein was extracted with M-PER mammalian protein extraction

reagent (78501, Thermo Fisher Scientific, Waltham, MA) and sonicated. Western blotting was performed with a NuPAGE system (Invitrogen) using rabbit anti-human WISP1 polyclonal antibodies known to cross-react with mouse material at 1:500 dilution (sc-25441, Santa Cruz Biotechnology, Santa Cruz, CA) and 1:2000 dilution (antibody LF-187, Dr. Larry W. Fisher, National Institutes of Health) and analyzed using a LI-COR imaging system (LI-COR Biosciences, Lincoln, NE).

For analysis of TRAF6, osteoclast cultures were prepared as described above, and protein was extracted on day 5 of culture using M-PER lysis buffer supplemented with Complete protease inhibitor mixture and PhosphoSTOP (11873580001 and 04906837001, respectively; Roche Diagnostics). Western blotting was performed with anti-TRAF6 antibody (1:1000 dilution; 8028, Cell Signaling Technology) and anti-HSP90 antibody (1:1000 dilution; 7947, Santa Cruz Biotechnology). In both cases, goat anti-rabbit secondary antibody (LI-COR Biosciences) was used.

For analysis of active (unphosphorylated) and total forms of β-catenin, BMSCs were cultured, and protein was extracted as described above. Western blotting was performed using antibodies against non-phosphorylated (active) β-catenin (1:1000 dilution; 8814, Cell Signaling Technology), total β-catenin (0.5 μg/ml; AF1329, R&D Systems), and β-actin (1:1000 dilution; 8457, Cell Signaling Technology). Goat anti-rabbit and donkey anti-goat secondary antibodies (LI-COR) were used. Densitometric analysis was performed using Odyssey 2.1 software (LI-COR Biosciences).

SOST-LDL Receptor-Related Protein (LRP) Interaction

The ability of WISP1 to inhibit the intracellular activation of Wnt signaling was tested using the Leading Light sclerostin-LRP interaction screening system (Enzo Life Sciences, Farmingdale, NY) following the manufacturer's protocol. Briefly, different concentrations of recombinant WISP1 (1, 5, 10, 25, and 50 μg/ml) were mixed with the LRP5-alkaline phosphatase fusion protein and incubated in triplicates in 96-well plates with immobilized baculovirus-expressed human sclerostin for 2 h at room temperature while shaking. After extensive washing, alkaline phosphatase substrate reagent was added to the wells and incubated for 25 min at room temperature. The intensity of the chemiluminescence reaction was then read using a chemiluminescence microplate reader (Centro XS^3 LB 960, Berthold Technologies GmbH, Bad Wildbad, Germany).

Dual-energy X-ray Absorptiometry (DXA)

Male and female WT or *Wisp1*$^{-/-}$ mice (1, 3, and 9 months old) were killed, weighed and scanned with a DXA machine (Lunar PIXImus densitometer, GE Healthcare) to determine the total bone mineral density (BMD). When analyzing the BMD, the skulls were excluded from the region of interest.

Micro-computed Tomography (μCT)

Femurs were dissected from 3-month-old male and female WT or *Wisp1*$^{-/-}$ mice, fixed with 4% paraformaldehyde for 48 h, and stored in 70% ethanol at 4 °C. They were then scanned and reconstructed with 8-μm isotropic voxels by μCT (eXplore Locus, GE Healthcare). Morphometric analysis was performed with eXplore MicroView software (GE Healthcare). The trabecular and cortical areas were analyzed separately, as shown in Fig. 3*A*.

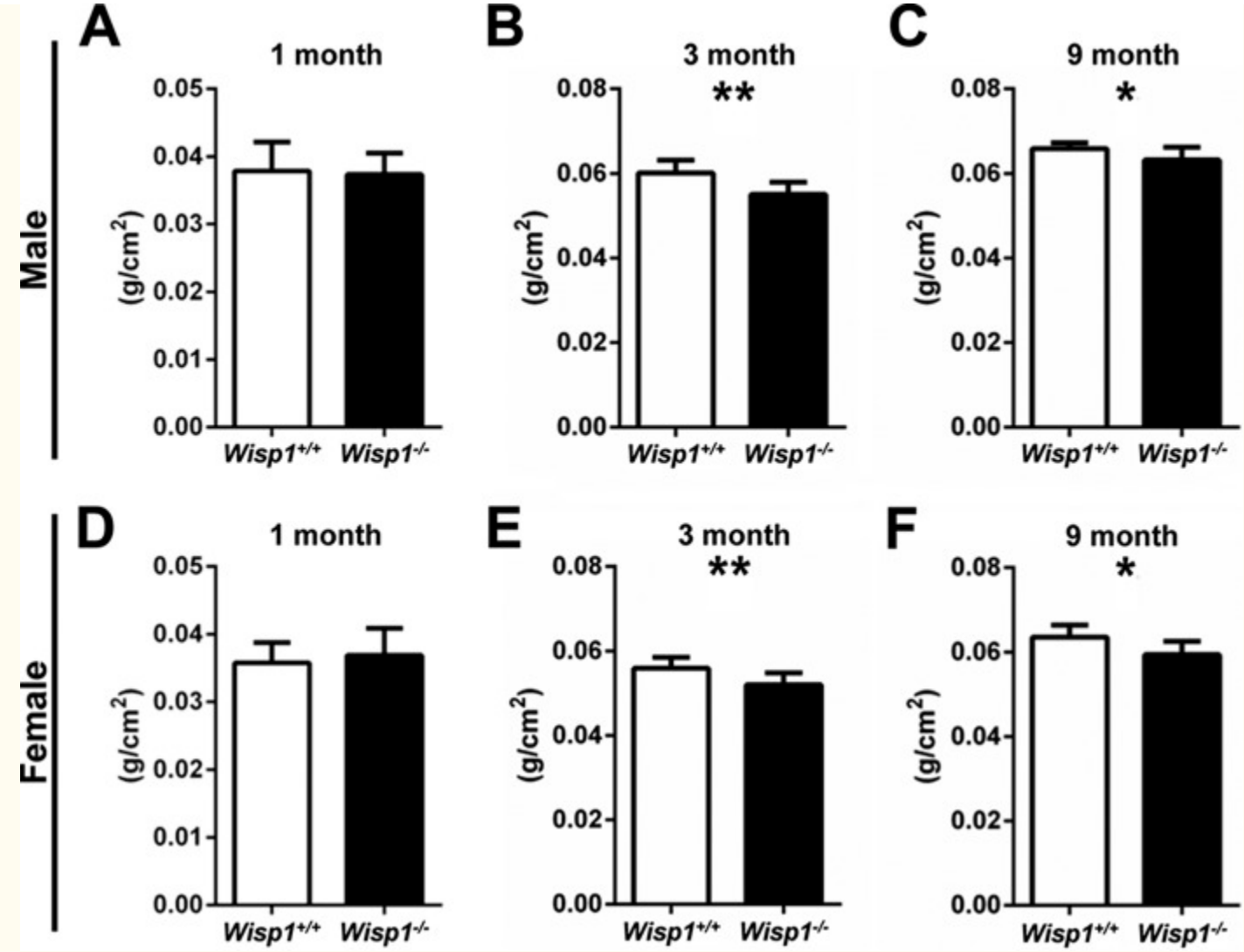

FIGURE 3.

Whole-body BMD of 1-month-old (*A* and *D*), 3-month-old (*B* and *E*), and 9-month-old (*C* and *F*) males (*A–C*) and females (*D–G*). Data are reported as mean ± S.D. (n = 7–10). *, $p < 0.05$; **, $p < 0.01$ *versus* the wild-type (+/+) sample.

Dynamic Labeling

Thirteen days prior to killing, calcein (25 μg/g of body weight) was intraperitoneally injected into 6–7-week-old female WT or *Wisp1*$^{-/-}$ mice. Twelve days later, tetracycline (20 μg/g of body weight) was intraperitoneally injected, the mice were killed the following day, and labeled tibias were collected. Bones were fixed with 4% paraformaldehyde for 48 h and embedded in methyl methacrylate. Samples were sectioned horizontally, and the distance between the two labels was measured at the endocortical surface using OsteoMeasure software (OsteoMetrics, Decatur, GA).

Bone Mechanical Strength Testing

Three-month-old male and female WT and *Wisp1*$^{-/-}$ mice were killed, and the femurs were harvested, stripped of soft tissue, wrapped in gauze soaked in calcium-buffered saline solution, and stored at −80 °C until analyzed. Thawed and hydrated femurs were tested by 4-point bending with the anterior surface in tension (3-mm loading span, 9-mm support span) at a cross-head displacement of 0.025 mm/s until catastrophic fracture using an eXpert 450 universal testing machine (n = 14–19/group; ADMET, Norwood, MA). Load and displacement were recorded during each test, and custom MATLAB scripts were used to

quantify stiffness, yield force, and ultimate force for each test. The procedures used were described in detail previously (10).

Colony-forming Efficiency Assay

Cells were flushed from bone marrow from 6–8-week-old female WT or *Wisp1*$^{-/-}$ mice; plated in 25-cm^2 flasks (1.0 × 10^6 cells/flask) with α-minimal essential medium containing 20% lot-selected FBS, 100 units/ml penicillin, 100 μg/ml streptomycin, 2 mM glutamine, and 0.1 mM 2-mercaptoethanol; and cultured for 10 days without a medium change. At the end of cultivation, cells were rinsed with Hanks' balanced salt solution (14170, Gibco) and fixed with 100% methanol for 30 min. Cells were stained with an aqueous solution of saturated methyl violet for 30 min, and unbound stain was removed by washing the cells three times with distilled water. After drying, the number of colonies each originating from a single colony-forming unit-fibroblast with >30 cells was evaluated using a dissecting microscope.

Transplantation of BMSCs

Gelfoam (Pfizer) was cut into uniform pieces (5 × 5 × 7 mm^3), saturated with WT or *Wisp1*$^{-/-}$ BMSCs (2.0 × 10^6 cells/piece), and transplanted into the subcutaneous tissue of the upper backs of immunocompromised Athymic Nude-*Fox1*^{nu} mice. After 6 weeks, ectopic ossicles were harvested, fixed with 4% paraformaldehyde, and analyzed by μCT and histology.

Ovariectomy

Eight-month-old female WT and *Wisp1*$^{-/-}$ mice were anesthetized with a combination of ketamine (150 mg/kg), xylazine (9 mg/kg), and acepromazine (5 mg/kg) or isoflurane (2–5% in O_2). A 1-cm incision was made on the back along the vertebrae to open the peritoneum and allow access to the abdominal cavity. The exposed ovaries on both sides were removed, the abdominal cavity was closed by re-apposing the posterior abdominal muscles, and the skin incision was closed with tissue glue. Four weeks after surgery, mice were subjected to DXA scans, and the whole-body BMD was determined.

Histology

Deparaffinized and hydrated sections were stained with Safranin O or a Picrosirius Red stain kit (797, Polysciences, Warrington, PA). Hematoxylin was used as for counterstaining. For TRAP staining, consecutive deparaffinized and hydrated sections were stained with a TRAP kit (294-67001, Wako Pure Chemical Industries, Osaka, Japan) following the manufacturer's recommendations.

Immunohistochemistry

Deparaffinized and hydrated sections were blocked with 3% hydrogen peroxide to quench endogenous peroxidase activity and blocked with 10% normal rabbit serum for 1 h at 37 °C. The primary antibody against total β-catenin (5 μg/μl) and the negative control (goat IgG, 5 μg/μl) were added to sections and incubated overnight at 4 °C. The samples were then incubated with HRP-conjugated rabbit anti-goat secondary antibody (1:1000 dilution; 14-13-06, KPL) for 30 min at room temperature and detected with aminoethyl carbazole (00-1111, Life Technologies, Inc.). Samples were counterstained with Mayer's hematoxylin and imaged using an Aperio ScanScope slide scanner.

Statistical Analysis

An unpaired *t* test was performed to compare WT and *Wisp1*$^{-/-}$ samples using GraphPad Prism 6 software (GraphPad Software, La Jolla, CA). $p < 0.05$ was considered significantly different.

Results

Generation of Wisp1-deficient Mice

A DNA construct with a PGK-neo cassette inserted into exon 2 was used to target the *Wisp1* allele in ES cells using standard procedures (Fig. 1*A*). Two ES clones, 3H4 and 4C5, were identified after restriction digestion with ApaI, followed by Southern blotting using an external BglI probe, and were subsequently used for injection of blastocysts to create chimeric mice. Both ES clones transmitted the targeted allele to offspring. The positive line (3H4) was selected for further analysis. To examine the relative *Wisp1* levels in the mutant mice, we first isolated mRNA from the calvarias of 3-day-old WT and *Wisp1*$^{-/-}$ mice or from BMSCs isolated from 6-week-old mice and analyzed the relative levels of *Wisp1* by Northern blotting (Fig. 1*B*) and real-time PCR (*Fig.* 1*C*). Both procedures showed that *Wisp1*$^{-/-}$ osteogenic cells had significantly reduced *Wisp1* mRNA compared with WT cells. Protein isolated from long bones (Fig. 1*D*) or osteoblastic cells (Fig. 1*E*) analyzed by Western blotting also showed that *Wisp1*$^{-/-}$ mice had significantly reduced WISP1 protein, leading us to conclude that this new model is null for *Wisp1* mRNA and protein production.

Effect of Wisp1 Deficiency on Body Weight and Length

Up until 1 month of age, the *Wisp1*$^{-/-}$ mice appeared normal and healthy (Fig. 2*A*), but female *Wisp1*$^{-/-}$ mice weighed slightly less than the WT counterparts (Fig. 2*C*). When the lengths of WT and *Wisp1*$^{-/-}$ mice were measured at 3 months of age from the top of the head to the base of the tail, both males and females showed a slight but significant reduction in size (Fig. 2*B*). Analysis of the growth plates of growing mice at embryonic day 18.5 showed that the hypertrophic zone of growth plate was expanded in the *Wisp1*$^{-/-}$ mice compared with the WT mice (Fig. 2, *D–F*).

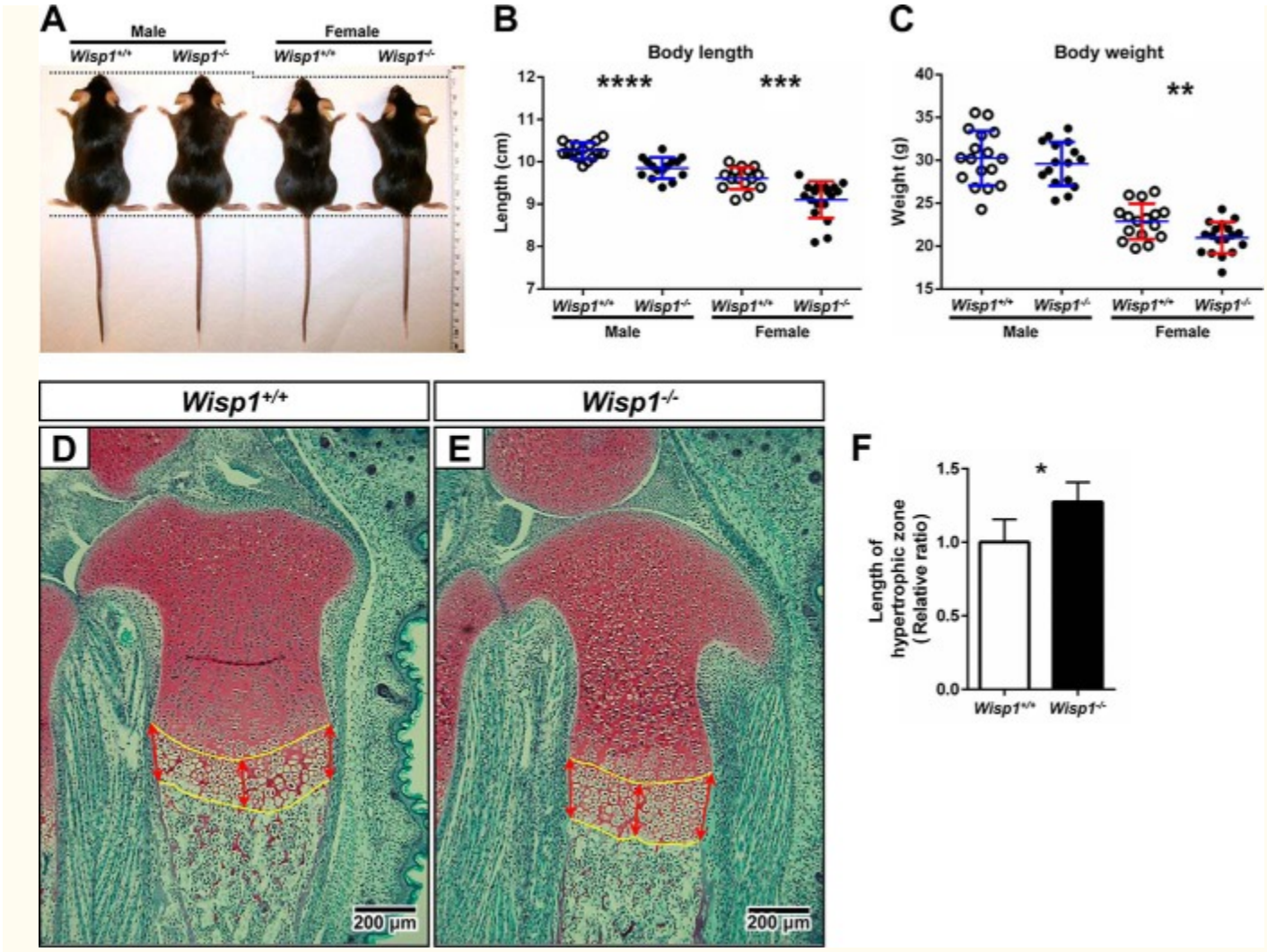

FIGURE 2.

A, representative images of male and female *Wisp1*$^{+/+}$ (WT) and *Wisp1*$^{-/-}$ mice at 3 months of age. *B*, whisker plot of body length of 3-month-old mice (n = 16–18). Each *dot* represents an individual mouse whose body length was measured from the top of the head to the base of the spine. ***, $p < 0.001$; ****, $p < 0.0001$ versus the wild-type (+/+) sample for the same gender. *C*, weight of WT mice compared with *Wisp1*$^{-/-}$ mice shown in a whisker plot. **, $p < 0.01$ *versus* the wild-type (+/+) sample. *D* and *E*, representative sections through growth plates of WT and *Wisp1*$^{-/-}$ mice, respectively. *Red arrows* point to regions of the growth plate selected for measurements of the hypertrophic zone shown in *F*. *, $p < 0.05$ *versus* the wild-type (+/+) sample. Data are reported as mean ± S.D. (n = 7–10).

Effect of Wisp1 on BMD

To determine the potential role of WISP1 in the skeleton, whole-body DXA scans were performed. At 1 month of age, there were no significant differences in BMD (g/cm^2) between male (Fig. 3*A*) and female (Fig. 3*D*) WT and *Wisp1*$^{-/-}$ mice. By 3 months, however, both male (Fig. 3*B*) and female (Fig. 3*E*) *Wisp1*$^{-/-}$ mice had statistically reduced BMD compared with WT controls, and these differences persisted until 9 months of age (Fig. 3, *C* and *F*). These DXA analyses indicated that knocking out/ablating WISP1 had a global effect on total BMD, but they did not reveal precisely how different regions of the bones were affected. For that reason, long bones were isolated from the WT and *Wisp1*$^{-/-}$ mice and analyzed further by three-dimensional μCT.

Skeletal Phenotyping of Wisp1$^{-/-}$ *Bones*

Three-dimensional images of femurs from 3-month-old mice were acquired by μCT scanning, and the trabecular and cortical regions were analyzed separately as shown in Fig. 4*A*. In the trabecular region, a 1.0-mm-long cylinder located 0.5 mm proximally from the distal growth plate was delineated as a region of interest, with dimensions of 0.8 × 1.3 mm (Fig. 4*A*). The BMD, bone volume/total volume (BV/TV), trabecular number, trabecular thickness, trabecular separation, and connectivity density within the region of interest were subsequently measured in male and female mice. This analysis showed that the BMD (Fig. 4*B*) and trabecular number (Fig. 4*D*) were significantly reduced, but only in the female *Wisp1*$^{-/-}$ mice. Trabecular separation was significantly increased in female *Wisp1*$^{-/-}$ mice compared with WT controls (Fig. 4*F*). Other parameters that were not significantly different included BV/TV (Fig. 4*C*) and trabecular thickness (Fig. 4*E*). Connectivity density, known to be variable in the trabecular bone, also did not show significant differences between *Wisp1*$^{-/-}$ and WT mice (data not shown). For cortical bone analysis, the region of interest was located 0.5 mm distally from the midshaft of the bone and encompassed a 1.0-mm cylinder with dimensions of 2.5 × 2.5 mm (Fig. 4*A*), and the cortical thickness and cross-sectional area were measured within this area. This analysis showed that both male and female *Wisp1*$^{-/-}$ mice had significantly reduced cortical thickness (Fig. 4*G*) and cross-sectional area (Fig. 4*H*) compared with a comparable region in WT mice.

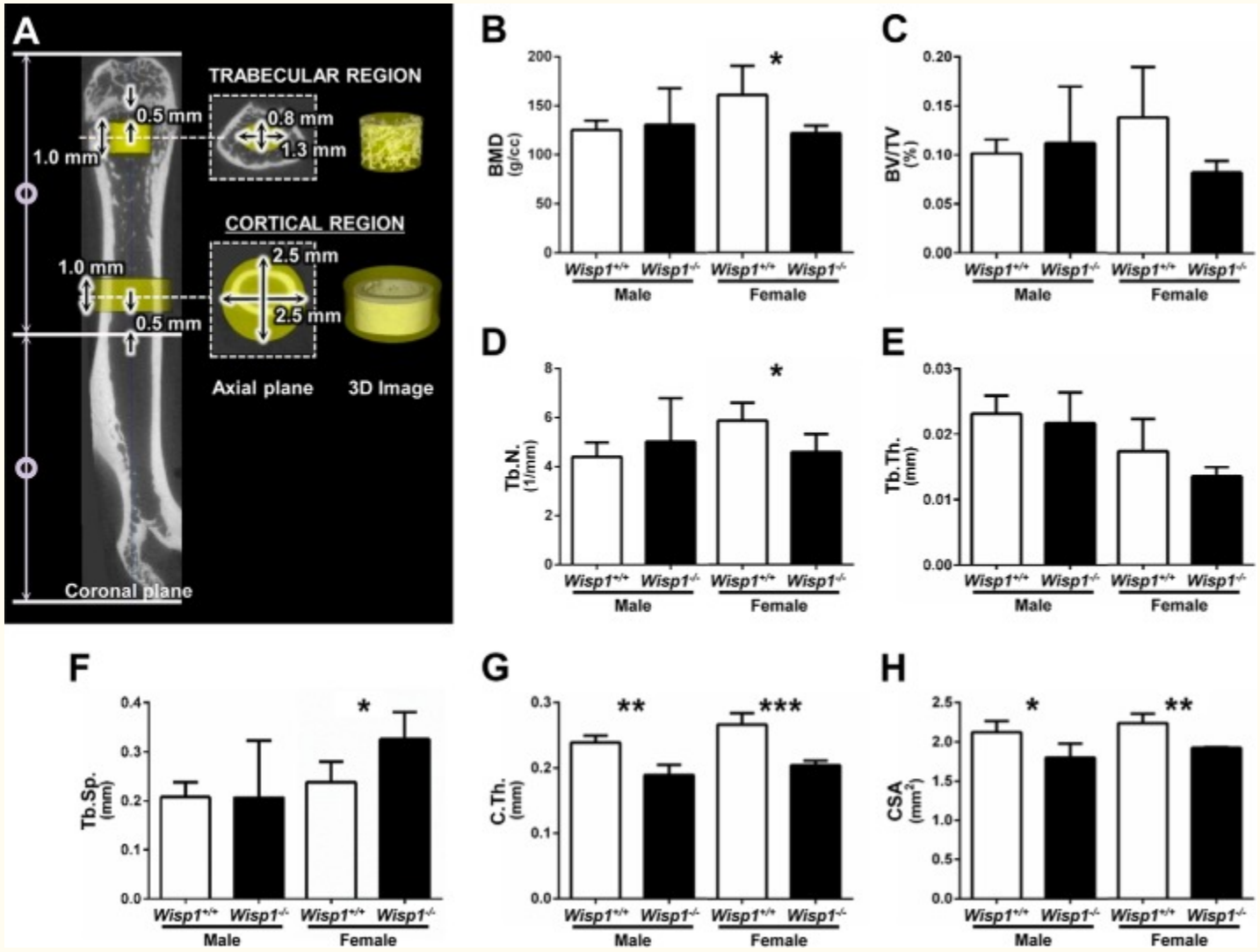

FIGURE 4.

μCT analysis of femurs from 3-month-old WT and *Wisp1*$^{-/-}$ males and females. *A*, femurs were separately analyzed in the trabecular region (elliptic cylinder of 0.8 mm in the minor axis × 1.3 mm in the major axis × 1.0 mm

in height) and in the cortical region (cylinder of 2.5 mm in diameter × 1.0 mm in height). Parameters for the trabecular region are as follows: BMD (*B*), BV/TV (*C*), trabecular number (*Tb.N.*; *D*), trabecular thickness (*Tb.Th.*; *E*), and trabecular separation (*Tb.Sp.*; *F*). Parameters for the cortical region are as follows: cortical thickness (*C.Th.*; *G*) and cross-sectional area (*CSA*; *H*). Data are reported as mean ± S.D. ($n = 4$). *, $p < 0.05$; **, $p < 0.01$; ***, $p < 0.001$ *versus* the wild-type (+/+) sample.

Effect of Wisp1 Deficiency on Biomechanical Strength

Because we found differences in cortical thickness between *Wisp1*$^{-/-}$ and WT mice, we wondered if the biomechanical strength of the bones would be affected by WISP1 deficiency. To test this, bones from 3-month-old male and female WT and *Wisp1*$^{-/-}$ mice were subjected to 4-point bending, and the amount of force needed to bend (stiffness and yield force) and break (ultimate force) was measured. As we predicted from the μCT data, both male and female *Wisp1*$^{-/-}$ mice had significantly reduced levels of stiffness, yield force, and ultimate force needed to deform the bones compared with WT counterparts (Table 2). Taken together, these data show that the reduced cortical thickness seen in *Wisp1*$^{-/-}$ mice led to reduced stiffness, which was accompanied by a reduction in mechanical strength.

TABLE 2

A 4-point bending test performed with femurs from 3-month-old male and female WT or *Wisp1*$^{-/-}$ mice

N, newtons.

Mice	*n*	Stiffness (N/mm)	Yield force (N)	Ultimate force (N)
Male				
Wisp1$^{+/+}$	17	211.88 ± 34.37	27.09 ± 5.38	36.15 ± 6.53
Wisp1$^{-/-}$	14	165.65 ± 47.21[a]	22.50 ± 4.24[b]	25.92 ± 5.31[c]
Female				
Wisp1$^{+/+}$	16	148.53 ± 32.66	25.02 ± 5.22	28.04 ± 3.26
Wisp1$^{-/-}$	18	115.03 ± 24.93[a]	19.21 ± 3.17[c]	21.91 ± 3.02[c]

[a] $p < 0.01$ *versus* wild-type (+/+) sample for the same gender.

[b] $p < 0.0$ *versus* wild-type (+/+) sample for the same gender.

[c] $p < 0.001$ *versus* wild-type (+/+) sample for the same gender.

Picrosirius Red Staining of Bone Collagen

To further assess the character of the bones from the *Wisp1*$^{-/-}$ mice, we sectioned and stained femurs with Picrosirius Red, a dye that binds to collagen and reveals changes in collagen assembly. We pursued this point because we found that *Wisp1*$^{-/-}$ BMSCs made substantially less *Col1A1* compared with WT BMSCs (Fig. 5*I*). Fig. 5 (*A*, *B*, *E*, and *F*) shows a composite of sections assembled from representative WT and *Wisp1*$^{-/-}$ femurs. When examined at higher power with visible light, the thinner cortexes of the *Wisp1*$^{-/-}$ mice are apparent (Fig. 5, *C* and *D*). To obtain a better view of collagen fibrils in the *Wisp1*$^{-/-}$ bones, the same sections were visualized using polarized light (Fig. 5, *E–H*). This analysis highlighted that the collagen staining was reduced in *Wisp1*-deficient bones and could potentially contribute to their decreased biomechanical strength.

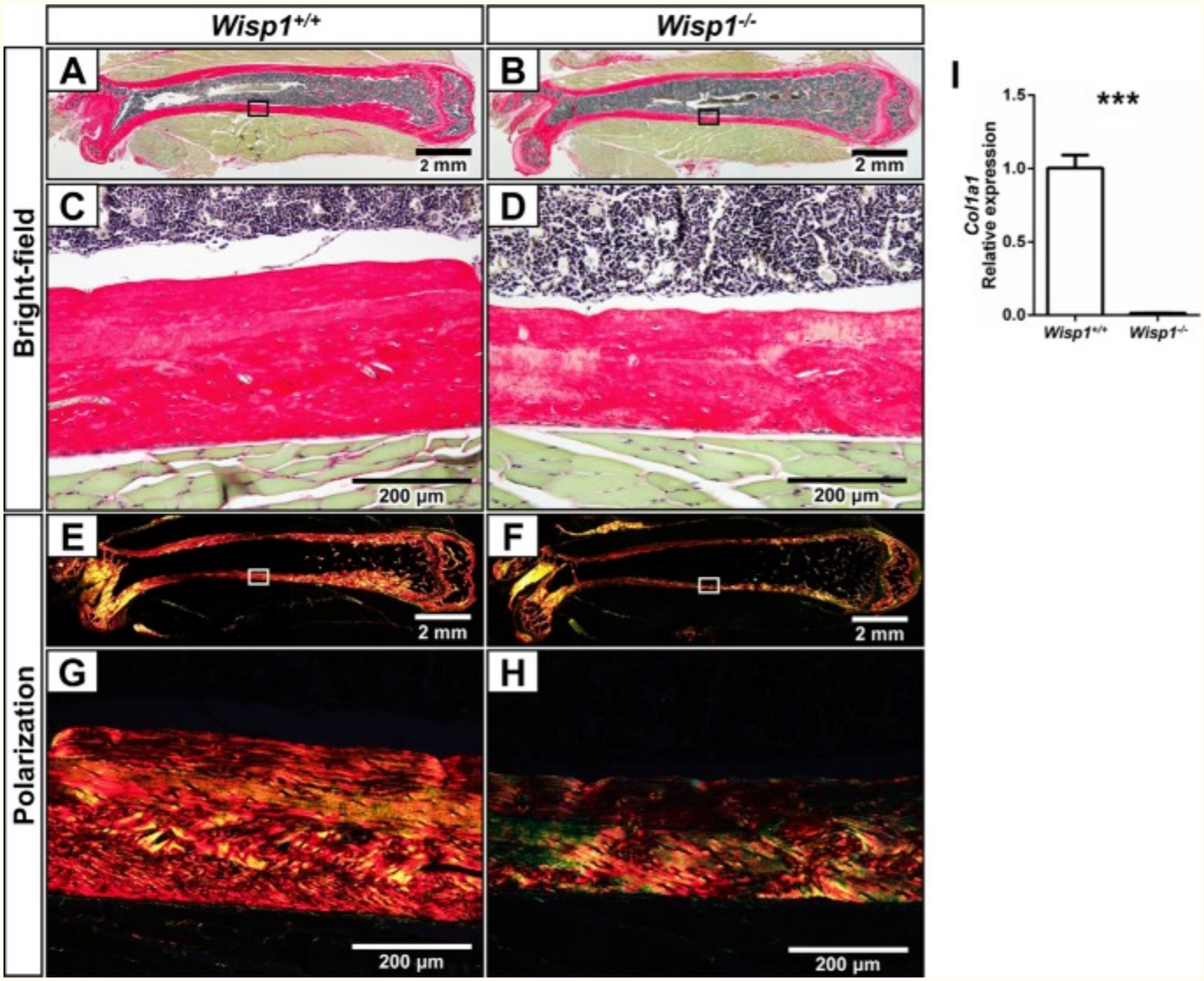

FIGURE 5.

Effect of *Wisp1* deficiency on collagen expression and organization. Femurs from 3-month-old WT (*A*, *C*, *E*, and *G*) or *Wisp1*$^{-/-}$ (*B*, *D*, *F*, and *H*) females were stained with Picrosirius Red: bright-field (*A–D*) and with

polarization (*E–H*). *A*, *B*, *E*, and *F*, composite of the bones used. The *boxed areas* within the composites are shown in higher power (*C*, *D*, *G*, and *H*). *I*, BMSCs were isolated from WT and *Wisp1*$^{-/-}$ mice and grown in osteogenic inducing medium for 2 weeks, after which mRNA was extracted and used for quantitative PCR of *Col1A1*. ***, $p < 0.001$ *versus* the wild-type (+/+) sample.

Dynamic Labeling and Histomorphometry

To determine the relative rate of bone formation in the *Wisp1*$^{-/-}$ mice, dynamic histomorphometry was performed. Six-week-old mice were first injected with the fluorochrome calcein, followed by a second injection of tetracycline 12 days later. Both of these agents incorporate into sites of new bone formation. In our analysis, we focused on endocortical bone formation because we found the greatest differences in this region by μCT. Fig. 6 (*A* and *B*) shows a bright-field view of representative bones, which were subsequently visualized by fluorescence under low power (*C* and *D*) and under higher power (*E* and *F*). When the distance between the two labels was measured on the endocortical surface, we found a significant reduction in endocortical mineral apposition rate (Fig. 6*G*) in the *Wisp1*$^{-/-}$ mice compared with control mice, with a trend toward a reduced endocortical double-labeled area (Fig. 6*H*). From these data, we suspected that bone-forming cells were defective in *Wisp1*$^{-/-}$ mice, possibly arising from a deficiency in the function of osteogenic progenitors. To address this, we next examined the biological activity of osteogenic cells from WT and *Wisp1*$^{-/-}$ mice for numerous parameters, including colony-forming efficiency, osteoblast and osteoclast differentiation *in vitro*, and differentiation *in vitro* in transplants.

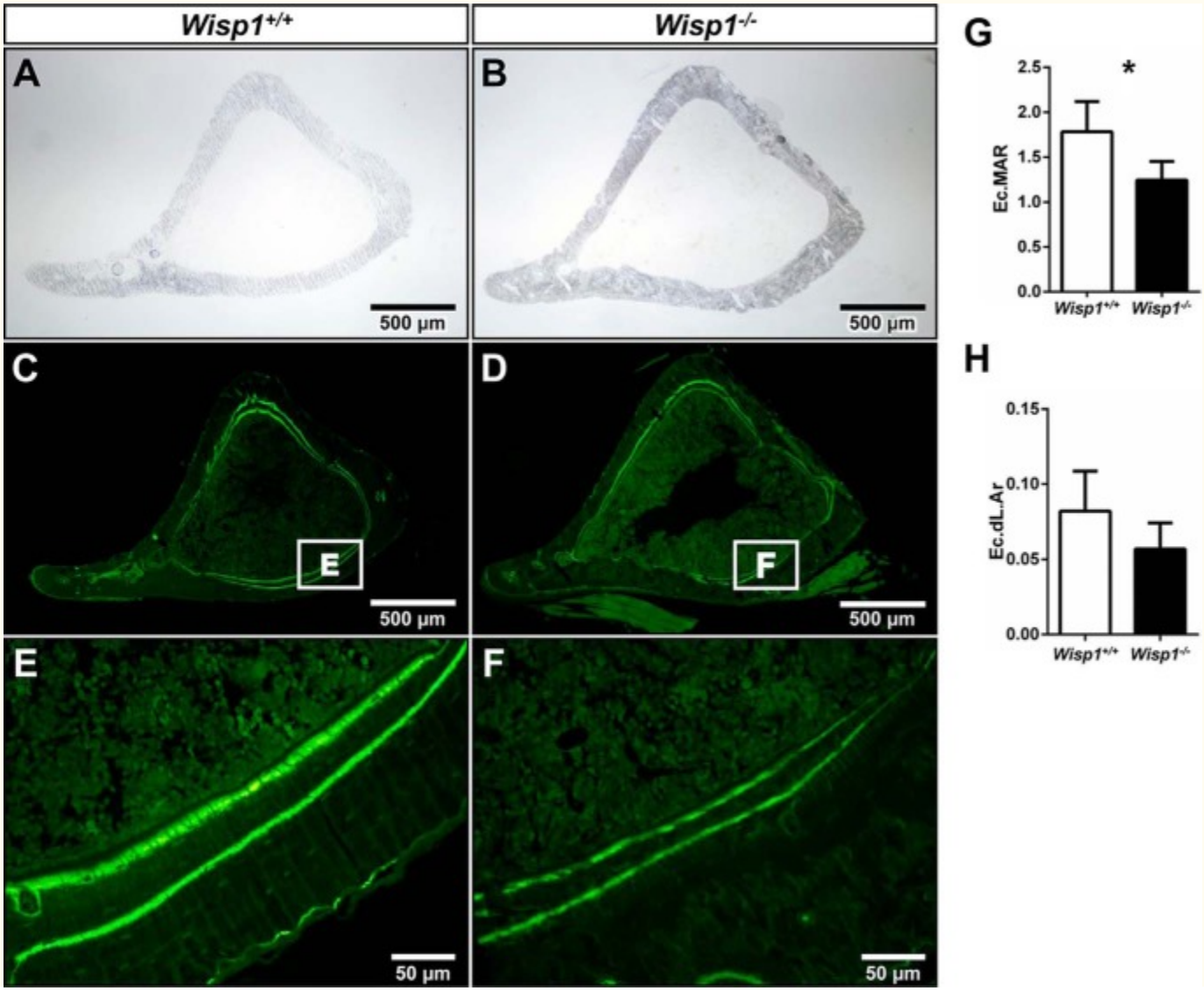

FIGURE 6.

Dynamic histomorphometric analysis. Calcein and tetracycline were injected into 5-week-old WT and *Wisp1*$^{-/-}$ females 13 days and 1 day prior to killing. Shown are representative bright-field sections of tibias from WT (*A*) and *Wisp1*$^{-/-}$ (*B*) mice. The same sections are shown visualized under fluorescent light (*C–D*). The *boxed areas* viewed under higher power in *E* and *F* show representative double labels used for tracing with the upper/inside band from the tetracycline label and the lower/outside band from the calcein label. *G*, endocortical mineral apposition rate (*Ec.MAR*). *H*, endocortical double-labeled area (*Ec.dL.Ar*). *, $p < 0.05$ *versus* the wild-type (+/+) sample.

Colony-forming Efficiency and Osteogenic Differentiation of BMSCs

To study skeletal cell functions in WISP1 depletion, we first estimated osteoprogenitor cell number by comparing the number of colonies initiated by the colony-forming unit-fibroblast in WT mice *versus* *Wisp1*$^{-/-}$ mice. Fig. 7*A* shows representative stains of the colonies formed by WT (*left*) and *Wisp1*$^{-/-}$ (*right*) cells, which were counted and depicted graphically in Fig. 7*B*. In eight separate experiments, we found no difference in number between WT and *Wisp1*$^{-/-}$ cells, implying that the overall progenitor number is not affected by WISP1 deficiency. To test the function of the osteoblast progenitors, we cultured them in osteogenic medium and analyzed the expression of mRNAs encoding alkaline phosphatase, bone sialoprotein, and osteocalcin, which are osteogenic markers that progressively represent early-to-late stages of maturation, respectively. All three mRNAs were significantly reduced in *Wisp1*$^{-/-}$ cells compared with WT cells (Fig. 7, *C–E*), implying their diminished ability to differentiate. In agreement with this finding, we saw reduced accumulation of Ca^{2+} at similar stages of the induced osteogenesis *in vitro* in WISP1-deficient cells (Fig. 7*F*) compared with WT cells. Addition of recombinant WISP1 to the cultures reversed this defect (Fig. 7*G*). The above observations suggested that WISP1 deficiency could affect the osteogenic function of BMSCs.

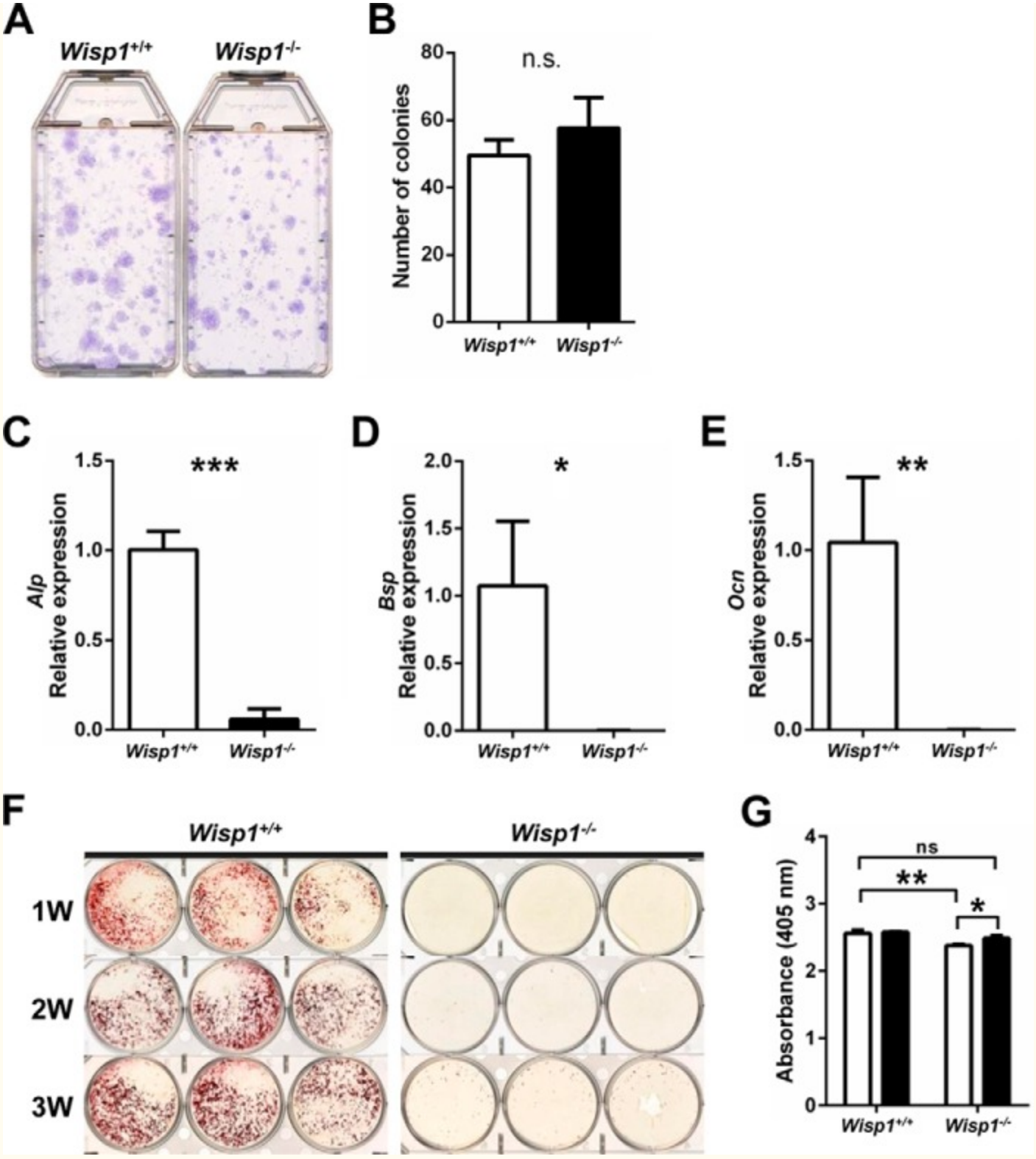

FIGURE 7.

Effect of *Wisp1* deficiency on colony-forming efficiency and the osteogenic differentiation of BMSCs. *A*, representative image of the number of colonies initiated by a single colony-forming unit-fibroblast formed in WT and *Wisp1*$^{-/-}$ mice. *B*, enumeration of colonies shown in *A. White bar*, WT; *black bar*, *Wisp1*$^{-/-}$. *C–E*, quantification of the relative expression levels of osteogenic differentiation markers measured by real-time PCR in WT and *Wisp1*$^{-/-}$ BMSCs cultured with osteogenic differentiation medium for 2 weeks: alkaline phosphatase (*Alp*; *C*), bone sialoprotein (*Bsp*; *D*), and osteocalcin (*Ocn*; *E*). *F*, Alizarin Red S staining of WT and *Wisp1*$^{-/-}$ BMSCs cultured with osteogenic medium for 1–3 weeks (*1W*, *2W*, and *3W*). *G*, relative levels of Alizarin Red accumulation

in cells cultured in the absence (*white bars*) and presence (*black bars*) of recombinant WISP1. *, $p < 0.05$; **, $p < 0.01$; ***, $p < 0.001$ *versus* the wild-type (+/+) sample. *n.s.*, not significant.

Effect of Wisp1 Deficiency on Osteogenic Differentiation

To learn more about the defective nature of the BMSCs from *Wisp1*$^{-/-}$ mice, we used an *in vivo* transplantation assay. In this experiment, BMSCs were first expanded *in vitro* and then placed in a collagen sponge, which was implanted under the skin of nude mice (11). Six weeks post-transplantation, ectopic ossicles formed, which contained a cortical shell of bone surrounding a marrow cavity with trabecular bone. Three-dimensional imaging of the transplants was first used to estimate the amount of new bone formed (Fig. 8, *A–D*), and when quantified, it showed that cells from *Wisp1*$^{-/-}$ mice had lower BMD, BV/TV, and trabecular number and increased trabecular space (trabecular separation) relative to transplants derived from WT BMSCs (Fig. 8, *U–X*). Trabecular thickness was not statistically different in the transplants from the *Wisp1*$^{-/-}$ and WT mice (Fig. 8*Y*). Histology of the transplants showed that they formed characteristic pink/lavender staining of bone with H&E staining (Fig. 8, *E* and *G*) and a Picrosirius Red-positive cortical shell surrounding Picrosirius Red-positive trabecular bone-like structures (Fig. 8, *F* and *H*). Closer inspection of the different regions of the transplant showed that those formed from *Wisp1*$^{-/-}$ cells had reduced cortical (Fig. 8, *I–L*) and trabecular (Fig. 8, *M–P*) Picrosirius Red-positive staining compared with WT cells. We also observed substantially more TRAP-positive cells in transplants derived from *Wisp1*$^{-/-}$ cells compared with those derived from WT cells (Fig. 8, *Q–T*). This suggested that the defective *Wisp1*$^{-/-}$ BMSCs in some way directly or indirectly affected osteoclast differentiation.

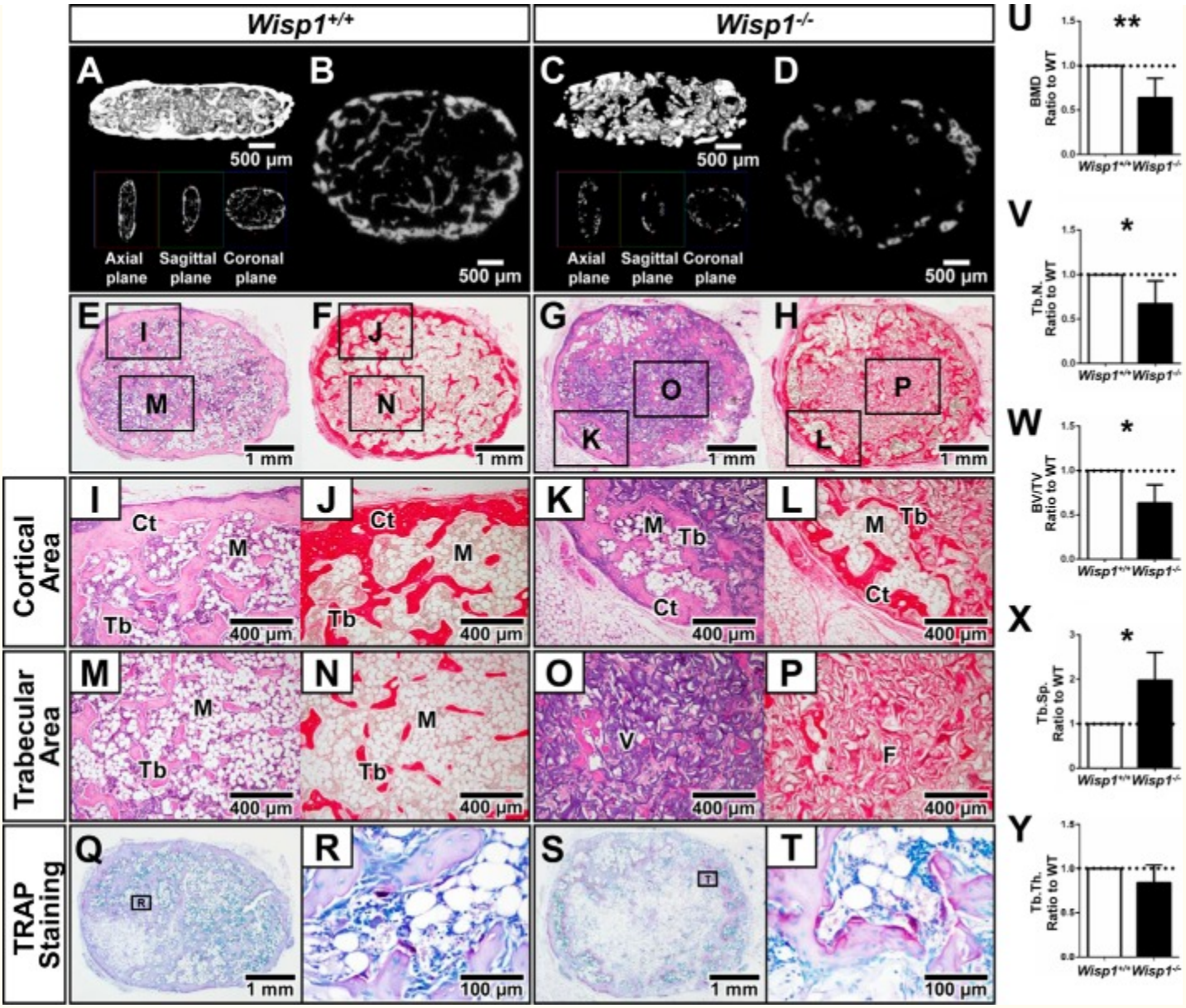

FIGURE 8.

Shown are µCT reconstructed three-dimensional images (*A* and *C*) and cross-sections of µCT images (*B* and *D*) of transplants formed from WT and *Wisp1*$^{-/-}$ BMSCs. H&E staining (*E* and *G*) and Picrosirius Red staining (*F* and *H*) were used to highlight collagen-rich regions of the transplant. Regional differences in transplants from WT and *Wisp1*$^{-/-}$ BMSCs with *boxed areas* are shown in higher power for both H&E and Picrosirius Red (*I–P*). Cortical (*Ct*) areas are shown in *I–L*, and trabecular (*Tb*) areas are shown in *M–P*. TRAP-stained WT (*Q* and *R*) and *Wisp1*$^{-/-}$ (*S* and *T*) transplants are shown under low (*Q* and *S*) and high (*R* and *T*) power. Shown are the results from evaluation of the structural parameters of the ossicles formed from WT and *Wisp1*$^{-/-}$ BMSCs, including BMD (*U*), trabecular number (*Tb.N.*; *V*); BV/TV (*W*), trabecular separation (*Tb.Sp.*; *X*), and trabecular thickness (*Tb.Th.*; *Y*). *M*, marrow; *F*, fibrous tissue; *V*, vehicle. Morphometric results are presented as the ratio of ossicles derived from *Wisp1*$^{-/-}$ BMSCs normalized to values obtained from WT BMSCs harvested from the same immunocompromised mouse ($n = 4$ for WT and *Wisp1*$^{-/-}$), *, $p < 0.05$; **, $p < 0.01$ *versus* the wild-type (+/+) sample.

Osteoclastogenesis by Cells from Wisp1$^{-/-}$ *Mice*

To understand more about the nature of the osteoclasts from *Wisp1*$^{-/-}$ mice, bone marrow cells were isolated and cultivated under conditions that induce osteoclastogenesis *in vitro*. This experiment showed that bone marrow precursors from *Wisp1*$^{-/-}$ mice developed significantly more TRAP-positive

multinucleated cells (Fig. 9*A*). Quantitative analysis of cells showed that the osteoclast numbers/well (Fig. 9*B*) were higher when the cells were derived from *Wisp1*-deficient mice and that these cells covered a larger surface area (Fig. 9*C*) and had an overall larger average size (Fig. 9*D*) than cells from WT mice. Osteoclast progenitors from *Wisp1*$^{-/-}$ mice were also able to erode a biomimetic made of hydroxylapatite (Fig. 9*E*) to a greater extent compared with WT cells, suggesting their increased activity. The mRNA expression of *Opg* and *Rankl* was decreased in *Wisp1*$^{-/-}$ cells, with *Opg* being reduced to a greater extent than *Rankl*, causing a net imbalance in the ratio of *Rankl/Opg* mRNA expression in the absence of WISP1 (Fig. 9, *F* and *G*). Analysis of the *Rankl* signaling target TRAF6 (Fig. 9*H*) showed an increased but not significant trend in the *Wisp1*$^{-/-}$ cells compared with WT cells. *Wisp1*$^{-/-}$ cells also had increased expression of mRNAs for *Rank*, *Trap5b*, *CtsK*, *CalcR*, *OSCAR*, and *NFATc1* (data not shown), providing further evidence of increased osteoclast differentiation. Taken together, these observations suggested that *Wisp1*$^{-/-}$ mice have an osteoclast imbalance, which was then tested by inducing osteoclastogenesis *in vivo*. We surgically removed the ovaries (ovariectomy) to induce bone turnover. As we predicted, DXA analysis indeed showed that following ovariectomy, the *Wisp1*$^{-/-}$ mice had lower BMD compared with WT mice (Fig. 9*H*), indicating that WISP1 could serve to reduce bone loss caused by increased bone turnover after ovariectomy.

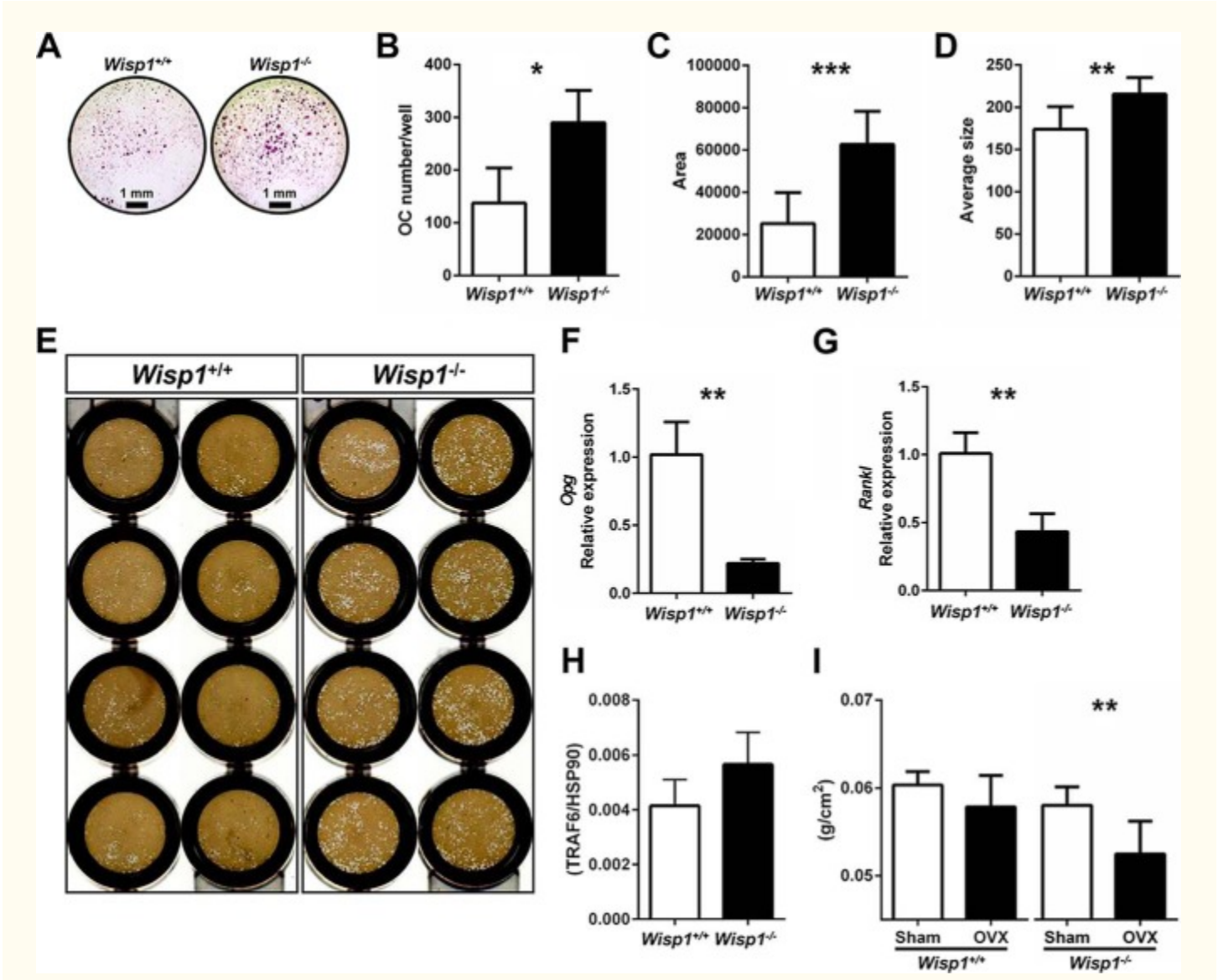

FIGURE 9.

Effect of *Wisp1* deficiency on osteoclastogenesis. *A*, TRAP staining of osteoclast progenitors derived from WT or *Wisp1*$^{-/-}$ bone marrow. *B–D*, quantification of results in *A*. *B*, osteoclast (*OC*) number/well. *C*, osteoclast area. *D*, average size of osteoclast formed. *, $p < 0.05$; **, $p < 0.01$; ***, $p < 0.001$ *versus* the wild-type (+/+). *E*, osteoclast precursors plated on osteo-mimetic OsteoAssay 96-well plates and cultured as described under "Experimental Procedures." *White spots* show areas eroded by the osteoclasts from WT (*left*) and *Wisp1*$^{-/-}$ (*right*) cells. Shown are the relative levels of *Opg* (*F*) and *Rankl* (*G*) mRNA expression and TRAF6 protein (*H*) in BMSCs isolated from WT (*white bars*) and *Wisp1*$^{-/-}$ (*black bars*) mice. **, $p < 0.05$ *versus* the wild-type (+/+) sample. *I*, whole-body BMD of 6-month-old ovariectomized (*OVX*) mice. **, $p < 0.01$ *Wisp1*$^{-/-}$ sham *versus Wisp1*$^{-/-}$ ovariectomy.

Altered Wnt Signaling in Wisp1$^{-/-}$ *Cells Is Partially Independent of LiCl Stimulation*

In the course of identifying downstream targets for WISP1 function, we analyzed multiple gene sets using gene array technology with a focus on the Wnt pathway, which is known both to regulate WISP1 and to be critical in bone function. When we examined BMSCs from WT and *Wisp1*$^{-/-}$ mice, we found that most Wnt target genes were constitutively down-regulated in the absence of WISP1 (data not shown). Quantitative real-time PCR analysis of several target genes confirmed our gene array data, including *Axin2* (Fig. 10*A*) and *Ccnd1* (Fig. 10*B*), which were significantly reduced in the *Wisp1*$^{-/-}$ cells. Considering that WISP1 is a secreted protein, we wondered whether promotion of Wnt signaling by inhibiting glycogen synthase kinase-3β (GSK) with LiCl would rescue the defect in Wnt signaling found in *Wisp1* deficiency. When the relative stimulation of expression of *Axin2* was measured after treatment of BMSCs with LiCl, we found a partial "rescue" of its expression (Fig. 10*C*), suggesting that Wisp1 could have complex means of regulating of Wnt signaling occurring both upstream and downstream of LiCl-induced inhibition of GSK. Both WT and *Wisp1*$^{-/-}$ cells responded to exogenous application of Wnt3A by up-regulating *Axin2* mRNA to the same extent in WT and *Wisp1*$^{-/-}$ cells (Fig. 10*D*). Taken together, these observations suggest that WISP1 and Wnt3A could have overlapping and connected functions outside the cell.

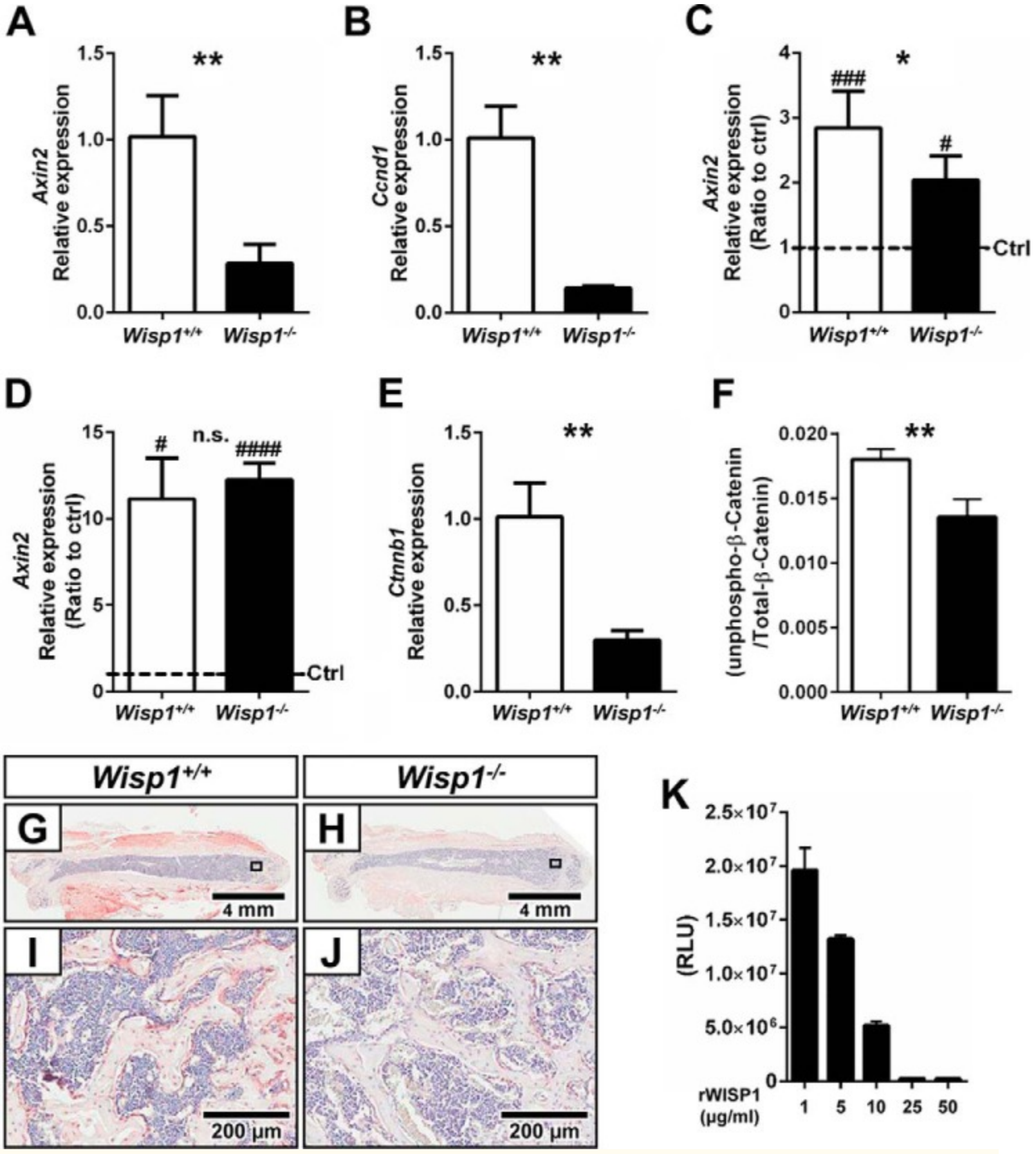

FIGURE 10.

Relative mRNA expression levels of Wnt signaling target genes. *A* and *B*, *Axin2* and *Ccnd1*, respectively, in BMSCs cultured with osteogenic differentiation medium for 1 week. *C*, mRNA expression level of *Axin2* in WT and *Wisp1*$^{-/-}$ BMSCs cultured in the presence or absence of LiCl for 4 days. *D*, results from the LiCl-treated group are shown as a ratio of control (*ctrl*) *versus* induced cells. *E*, relative levels of *Ctnnb1* mRNA in WT and *Wisp1*$^{-/-}$ BMSCs. *G*/*I* and *H*/*J*, relative levels of *Ctnnb1* mRNA in bone sections from WT and *Wisp1*$^{-/-}$ mice,

respectively. *F*, ratio of active unphosphorylated β-catenin to total β-catenin in WT and *Wisp1*$^{-/-}$ BMSCs. *K*, dose-dependent inhibition of SOST binding to LRP5 with increasing amounts of recombinant WISP1. *RLU*, relative light units; rWISP1, recombinant WISP1. *, $p < 0.05$; **, $p < 0.01$ *versus* the wild-type (+/+) sample; #, $p < 0.05$; ###, $p < 0.001$. *n.s.*, not significant.

Wisp1$^{-/-}$ *Cells Have Reduced β-Catenin Levels, Which May Arise from Inhibition of the SOST-LRP6 Interaction*

To understand more about the mechanism of WISP1 action, the levels of β-catenin were examined. As predicted from our analysis of Wnt target genes, we found that the levels of β-catenin mRNA (Fig. 10*E*) were significantly reduced in *Wisp1*$^{-/-}$ cells. β-Catenin was also reduced in the skeletal tissues of *Wisp1*$^{-/-}$ mice, determined by immunohistochemistry using antibodies to total β-catenin (Fig. 10, *G–J*). The level of active unphosphorylated/total β-catenin was also examined and was lower in *Wisp1*$^{-/-}$ cells compared with WT cells. Finally, when recombinant WISP1 was used in a Leading Light assay, it was found to inhibit functional binding of the inhibitor SOST to the Wnt receptor LRP5 in a dose-dependent manner (Fig. 10*K*).

Discussion

Previous work showed that WISP1 is up-regulated at sites of new bone formation and in osteoblastic cells induced to differentiate *in vitro* (6,–8). The goal of our investigation was to deepen our understanding of the role of WISP1 in bone *in vivo*. Toward this goal, a new mouse line was created in which *Wisp1* was depleted (*Wisp1*$^{-/-}$) and used to assess the function of WISP1 in regulating skeletal homeostasis. Our data point to roles for WISP1 in many aspects of bone formation, including regulating bone thickness and mineral density, as well as biomechanical strength. The skeletal cells dependent on WISP1 function are not only the BMSCs, in which WISP1 is highly expressed, but also osteoclasts, which are known to have an intimate relationship with osteogenic cells. We have also shown that the molecular foundation for WISP1-dependent bone cell and tissue activities may rely on functional Wnt signaling within the osteoblastic progenitors, which are needed for proper bone function.

Like all members of the CCN family, WISP1 has defined structural motifs that are conserved. The four different domains common to all members are 1) insulin-like growth factor-binding protein, 2) von Willebrand factor type C repeat, 3) thrombospondin type 1 repeat, and 4) cysteine-rich terminus. Considering the structural homology between the CCN members, it is not surprising that they share overlapping functions, including roles in cell migration and proliferation, integrin binding, and regulation of signal transduction (1). What is more intriguing are the unique aspects of each CCN member, whose activities seem to depend on the location of expression and the individual tissue context. Outlined below are examples that illustrate this latter point for members of the CCN family whose functions have been studied in detail in mineralized tissues, including CCN1, CCN2, and CCN3.

By far, the most extensively studied CCN protein in bone is CTGF/CCN2. Loss-of-function studies in mice (12, 13) showed that CCN2 is needed for proper bone development during embryogenesis. In mature mice, however, a different paradigm for CCN2 function emerges. In one study, CCN2 was overexpressed (*i.e.* gain of function) in mature osteoblasts under the control of the human osteocalcin promoter and resulted in impaired bone formation, leading to premature osteopenia (low bone mass) (14). When the opposite experiment was performed using the same osteoblast-specific human osteocalcin promoter to deplete CCN in bone (*i.e.* cell-specific loss of CCN2 function), there was a mild low bone mass phenotype found only in male mice at 6 months of age (15). These counterintuitive and seemingly contradictory findings emphasize the complexity of CCN2 function, which appears to work differentially pre- and postnatally and could furthermore be dependent on the fine-tuning of CCN2 expression in specific cell types.

Like CCN2, Nov/CCN3 is expressed in skeletal cells (16), with functions that appear to be equally complex. Total depletion of CCN3 in mice causes prenatal mild skeletal defects that are proposed to arise from accelerated osteoblast differentiation (17). On the other hand, overexpression of CCN3 in osteoblasts using the human osteocalcin promoter as the driver causes premature osteopenia, which may be triggered by reduced osteoblastogenesis (18). Early studies using the osteogenic cell line MC3T3 showed that CCN3 inhibits BMP-2/4 induction of osteogenesis presumably by binding to it and blocking its function (19, 20). A more recent report confirms the notion that CCN3 is an inhibitory factor in bone regeneration (21). A previous study claims that CCN3 increases BMP-2/4 and subsequent mineralization (22). The reasons for these discrepant results are not clear but could be due to the fact that the latter study applied CCN3 protein externally to the cultures, whereas the former ones used adenovirus infection to overexpress CCN2 from inside the cell. Thus, CCN3 may have functions potentially dependent on its levels of expression (over or under) with possible variability from where in the cell it is introduced. Studies performed *in vitro* indicate that the influence of CCN3 on osteoblast differentiation depends on functional Notch signaling (19) and integrin receptors, as well as ILK, p38, JNK, and AP-1 pathways (22).

The importance of Wnt signaling in regulating bone function is now widely accepted. When BMSCs were treated with Wnt3A to induce osteoblast differentiation, mRNA profiling revealed a significant up-regulation of Cyr61/CCN1 (23). ChIP further showed that CCN1 is a direct and early target of Wnt signaling (23). Interestingly, Kawaki *et al.* (8) showed that when CCN1, CCN2, CCN4, and CCN5 were added to osteoblast cultures, they each induced Wnt signaling, determined by the up-regulation of β-catenin. Our current work using BMSCs derived from *Wisp1*$^{-/-}$ mice confirms that WISP1 likely has a positive effect on Wnt signaling during osteogenesis. We conclude that CCN proteins that are targets of Wnt signaling could, in some cases, also regulate Wnt signaling. This kind of feed-forward regulation has also been previously reported for *Wisp1* in primary neurons undergoing toxic cell degeneration (24). In this case, *Wisp1* can autoregulate its own expression through the promotion of β-catenin activity (24). In our study on osteogenesis, we showed that *Wisp1*-depleted BMSCs could be partially rescued by treatment with LiCl, an intracellular GSK inhibitor. These data imply that there could be a connection between *Wisp1* and β-catenin output. Because this rescue worked only partially, further control coming from somewhere upstream of GSK degradation is implied. Interestingly, experiments using recombinant WISP1 showed that it could block functional binding of the Wnt inhibitor SOST to LRP5. This further implies that WISP1, which is a downstream target, might increase Wnt signaling by interfering with the SOST-LRP5 Wnt blockade. Whatever the case, additional experiments will be needed to decipher its exact mechanisms of action.

For many years, investigations on Wnt signaling and bone focused on its role in osteoblasts, which are known to be critical for bone formation. As predicted, the targeted disruption of β-catenin in bone cells using the *Col1A1* promoter led to mice with low bone mass (25). A more recent study showed that osteoclast precursors treated with Wnt3A or LiCl are inhibited in their ability to form TRAP-positive (osteoclast) cells (26). This suggests that Wnt stimulation of cells isolated from bone marrow can simultaneously stimulate osteoblasts and inhibit osteoclasts, leading to a net bone increase. In this regard, it may be interesting to test the effects of LiCl *in vivo* to learn more about the WISP1-Wnt axis *in vivo*.

Sclerostin is a protein made by osteocytes and is an inhibitor of Wnt signaling. Neutralizing antibodies to sclerostin have been generated and are being used to counteract the Wnt inhibitor properties of sclerostin (for review, see Ref. 27). Short-term application of anti-sclerostin antibody induces anabolic bone-forming activity, which leads to enhanced bone mass and strength and enhanced fracture repair (27). Interestingly, enhanced Wnt signaling by anti-sclerostin antibody not only stimulates bone formation but also inhibits bone resorption in humans. In this regard, it is tempting to speculate that the function of WISP1 in bone in some ways phenocopies anti-sclerostin antibody treatment, which simultaneously and reciprocally affects both osteoblast and osteoclast differentiation.

Despite the great strides in understanding factors that control bone function, there is still a need to identify new factors that could help improve bone quality and repair in situations in which there is an imbalance in bone remodeling. By generating mice deficient in WISP1, we have shown that WISP1 has dual roles in regulating both osteoblast and osteoclast differentiation, ultimately affecting bone structure and strength. Interestingly, we have shown that the factors that regulate WISP1 expression may also be controlled by WISP1 itself. Future work will be needed to unmask the nature of the complex circuitry that connects WISP1 to bone function.

*This work was supported, in whole or in part, by National Institutes of Health Intramural Research Program Grant 1 Z01 DE000379-21 from NIDCR (to M. O., K. H., L. L., T. M. K., V. K., M. L. N., P. G. R., and M. F. Y.), Award R01 AR056657 from NIAMS and Award T32 DE007057 from NIDCR (to E. M., B. M., M. A. T., and D. H. K.), and Award AR052686 from NIAMS (to K. M. L.). This work was also supported by a fellowship from the Japan Society for the Promotion of Science (to A. M.).

[2]The abbreviations used are:

ES

embryonic stem

BMSCs

bone marrow stromal cells

TRAP

tartrate-resistant acid phosphatase

LRP

LDL receptor-related protein

DXA

dual-energy x-ray absorptiometry

BMD

bone mineral density

μCT

micro-computed tomography

BV/TV

bone volume/total volume

GSK

glycogen synthase kinase-3β.